Atmospheric nitrogen deposition fluxes into coastal wetlands and their impacts on ecosystem carbon sequestration in East Asia

Jia Liu[1], Yan Zhang[1,2,3], Shenglan Jiang[1],Yuqi Xiong[1], Chenji Jin[1], Qi Yu[1], Weichun Ma[1]

[1]Shanghai Key Laboratory of Atmospheric Particle Pollution and Prevention, National Observations and Research Station for Wetland Ecosystems of the Yangtze Estuary, Department of Environmental Science and Engineering, Fudan University, Shanghai 200433, China

[2]MOE laboratory for National Development and Intelligent Governance, Shanghai institute for energy and carbon neutrality strategy, IRDR ICoE on Risk Interconnectivity and Governance on Weather/Climate Extremes Impact and Public Health, Fudan University, Shanghai 200433, China

[3] Shanghai Institute of Eco-Chongming (SIEC), Shanghai, 200062, China

Correspondence to: Yan Zhang (yan_zhang@fudan.edu.cn)

These Supplementary Materials include:

Supplementary Figure S1 and Table S1-S4.

1 Materials and method

1.1 Nitrogen emission inventory

This study categorizes the sources of NOx, NH_3, $PM_{2.5}$, and PM_{10} into land-based anthropogenic sources and maritime shipping sources. For land-based anthropogenic emissions, we employed publicly available emission inventories. For maritime shipping sources, we developed bottom-up emission inventories using a ship emission model based on Automatic Identification System (AIS) data.

Ship emission inventory

The shipborne metal emission inventory in this study was developed using a bottom-up approach based on real-time AIS data for the entire year of 2017 (Yuan et al., 2023; Feng et al., 2019). The inventory was established using a fuel consumption-based method, where emission factors for various species present in marine fuels were compiled and adjusted according to specific ship parameters. The resulting emissions were aggregated to generate the shipping-related nitrogen element emission inventory. The emission factors used in the calculations are listed in **Table S1** and are expressed in units of g $(kWh)^{-1}$. For cases where the engine load factor is below 20%, low-load adjustment factors for main engines are applied, as shown in **Table S2**.

Table S1. Emission factors for micropollutants from ships (unit: g $(kWh)^{-1}$)

Pollutants	Low-speed diesel engine	Middle-speed diesel engine	High-speed diesel engine
NO_x	18.1	14.1	13.2
NH_3	0.0049	0.0029	0.00023
$PM_{2.5}$	1.2788	1.2788	0.368
PM_{10}	1.39	1.39	0.4

Table S2. Main engine low load adjustment factor

Load factor（%）	NO_x	NH_3	$PM_{2.5}$	PM_{10}
1	11.47	5.99	19.17	19.17
2	4.63	3.36	7.29	7.29
3	2.92	2.49	4.33	4.33
4	2.21	2.05	3.09	3.09
5	1.83	1.79	2.44	2.44
6	1.6	1.61	2.04	2.04
7	1.45	1.49	1.79	1.79
8	1.35	1.39	1.61	1.61
9	1.27	1.32	1.48	1.48
10	1.22	1.26	1.38	1.38
11	1.17	1.21	1.3	1.3
12	1.14	1.18	1.24	1.24
13	1.11	1.14	1.19	1.19
14	1.08	1.11	1.15	1.15
15	1.06	1.09	1.11	1.11
16	1.05	1.07	1.08	1.08
17	1.03	1.05	1.06	1.06
18	1.02	1.03	1.04	1.04
19	1.01	1.01	1.02	1.02

The specific calculation methods and formulas for ship emissions

The ship emission model used in this study is based on the AIS database, and detailed information about the model has been documented in previous studies (Chen et al., 2017; Fan et al., 2016; Zhao et al., 2020). Since shipborne pollutant emissions primarily originate from main engines (ME), auxiliary engines (AE), and auxiliary boiler (AB), emissions of specific pollutants are calculated by multiplying the energy consumption of each engine (unit: kW·h) by the corresponding fuel-based emission factor (unit: g $(kWh)^{-1}$). The overall modeling approach can be summarized as follows: ships are classified based on their attribute information, and different parameters—including emission factors, load factors, and low-load adjustment factors—are assigned according to the type of engine and fuel used. These parameters are then combined with ship dynamic data (e.g., geographic coordinates, timestamps, and operational status) to compute the final ship emission inventory. Both the ship attribute information and dynamic data used in this process are sourced from the AIS database.

The engine's revolutions per minute (RPM) are used to determine the engine type. In this study, we adopt the same classification criteria as reported in previous research: if RPM > 1000 (Li et al., 2018), the ME is classified as a high-speed diesel engine (HSD); if 1000 ≥ RPM > 300, it is classified as a medium-speed diesel engine (MSD); and if RPM ≤ 300, it is classified as a slow-speed diesel engine (SSD). AEs are assumed to be of the MSD type. Furthermore, it is assumed that SSD-type MEs use heavy fuel oil (HFO), HSD-type MEs use marine distillate oil (MDO), MSD-type MEs use a combination of heavy fuel products (HFP) and MDO, and MSD-type AEs use marine gas oil (MGO).

The formula for calculating the nitrogen emissions inventory for each ship is shown in Equation (1):

$$E_{i,j,k,l} = \sum_{i=1}^{n} P_j \times LF_{j,l} \times T_{j,l} \times EF_{i,j,k} \times \frac{LLAF_j}{10^6} \quad (1)$$

where *i* denotes the pollutant species (NO_x, NH_3, $PM_{2.5}$, PM_{10}); *j* represents the engine type (ME, AE, or AB); *k* refers to the fuel type (MDO, MGO, or HFO); *l* indicates the operational mode (normal cruising, slow cruising, maneuvering, anchoring, or berthing); and *n* corresponds to the number of AIS reporting intervals. E is the calculated emission amount (in tons); P is the rated engine power (kW); LF is the engine load factor (%); T is the operating time (h); and EF is the emission factor for metallic elements (g $(kWh)^{-1}$). Considering that main engines operating under low-load conditions exhibit reduced combustion efficiency and consequently higher pollutant emissions, LLAF is applied when the load factor is below 20%.

1.2 WRF-CMAQ settling

The WRF model in this study was configured with the following physical parameterization schemes: the Pleim-Xiu land surface model (Xiu and Pleim, 2001); the Rapid Radiative Transfer Model for General Circulation Models (RRTMG) for both shortwave and longwave radiation processes (Clough et al., 2005); the Asymmetric Convective Model version 2 for PBL dynamics (Pleim, 2007); and the Kain-Fritsch cumulus parameterization scheme (Kain, 2004). MODIS land use data, categorized into 20 classes, were used to describe surface characteristics. For the CMAQ model configuration, the *aero7* aerosol module (Xu et al., 2018) and the cb6r5 gas-phase chemical mechanism (Amedro et al., 2020) were employed, which include detailed halogen chemistry (Lana et al., 2011; Sarwar et al., 2019). The M3Dry scheme was used to calculate dry deposition **错误!未找到引用源。** (Pleim and Ran, 2011); this scheme was updated in CMAQ version 5.4 to improve consistency with size-resolved aerosol observations (Pleim et al., 2022). Wet deposition was computed using the AQCHEM cloud chemistry module (Fahey et al., 2017). Initial and boundary conditions for the simulation domain were generated based on hemispheric seasonal average CMAQ outputs from the CMAS data repository (U.S. EPA: CMAQ Model Version 5.3 Input Data).

The simulation domain covered the East Asia region, as shown in Figure S1, with a horizontal grid resolution of 36 km × 36 km. Vertically, the model employed 27 terrain-following layers extending from the surface up to 100 hPa, with a surface layer thickness of approximately 40 meters. In the CMAQ model, two rows of grid cells were removed along the lateral boundaries of the WRF domain, resulting in a final d01 domain consisting of 257 × 117 grid cells.

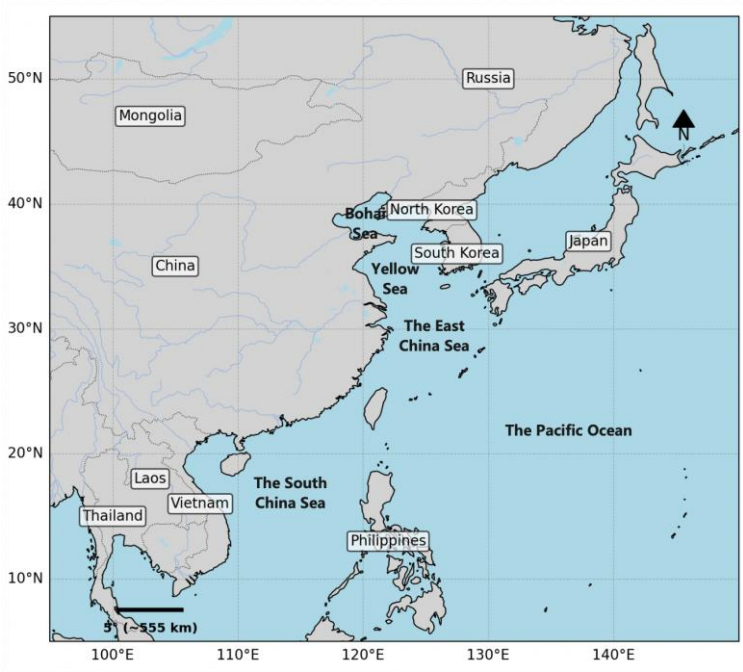

Figure S1. Simulation area of WRF-CMAQ

1.3 Solar radiation data

We extracted solar radiation data for various regions and wetland types across East Asia in 2017 from the Global High-Resolution (3-hourly, 10 km) Surface Solar Radiation Dataset (1983–2018, monthly) (Tang et al., 2019), provided by the National Tibetan Plateau Data Center of China. The resulting monthly average solar radiation values for different wetland types and regions in 2017 are summarized in **Table S3**, serving as input data for estimating carbon sequestration in wetlands.

Table S3. Monthly average solar radiation on different regions and types of wetlands, Unit: MJ m^{-2}

Area	Wetland type	SOLAR_Win.	SOLAR_Spr.	SOLAR_Sum.	SOLAR_Fal.
BS	Salt marsh	742.41	1695.95	1679.16	1055.16
	Mangrove forest	0.00	0.00	0.00	0.00
	Tidal flat	744.74	1692.19	1664.24	1049.17
YRD	Salt marsh	738.79	1401.52	1654.70	955.57
	Mangrove forest	729.42	1273.19	1733.28	1019.35
	Tidal flat	746.43	1406.60	1633.48	958.49
PRD	Salt marsh	937.28	1235.46	1760.36	1278.45
	Mangrove forest	930.04	1239.17	1749.29	1262.07
	Tidal flat	927.20	1233.00	1754.40	1265.40
BG	Salt marsh	719.53	1312.66	1681.56	1174.08
	Mangrove forest	735.03	1294.45	1631.53	1179.13
	Tidal flat	764.97	1330.96	1670.05	1198.93
KP	Salt marsh	792.88	1662.33	1648.57	1122.10
	Mangrove forest	0.00	0.00	0.00	0.00
	Tidal flat	766.64	1648.79	1624.92	1119.63
Kyushu	Salt marsh	745.30	1529.65	1753.77	995.29
	Mangrove forest	0.00	0.00	0.00	0.00
	Tidal flat	758.80	1515.62	1733.77	984.74

Table S4. The carbon sequestration capacity and oxygen release of different wetland types in different regions, Unit：g m^{-2}

Area	Wetland type	$Wco_{2\_Win.}$	$Wco_{2\_Spr.}$	$Wco_{2\_Sum.}$	$Wco_{2\_Fal.}$	$Wo_{2\_Win.}$	$Wo_{2\_Spr.}$	$Wo_{2\_Sum.}$	$Wo_{2\_Fal.}$
BS	Salt marsh	526.07	1201.74	1189.84	747.68	384.06	1400.80	1386.93	871.53
	Mangrove forest	0.00	0.00	0.00	0.00	0.00	0.00	0.00	0.00
	Tidal flat	51.94	118.03	116.08	73.18	37.92	137.58	135.30	85.30
YRD	Salt marsh	523.50	993.11	1172.51	677.11	382.19	1157.61	1366.73	789.27
	Mangrove forest	1160.59	2025.79	2757.83	1621.89	847.30	2361.35	3214.65	1890.55
	Tidal flat	52.06	98.11	113.93	66.85	38.01	114.36	132.80	77.93
PRD	Salt marsh	664.15	875.44	1247.38	905.90	484.87	1020.45	1454.00	1055.96
	Mangrove forest	1479.79	1971.65	2783.31	2008.08	1080.34	2298.24	3244.35	2340.71
	Tidal flat	64.67	86.00	122.37	88.26	47.21	100.24	142.63	102.88
BG	Salt marsh	509.85	930.14	1191.54	831.94	372.22	1084.22	1388.91	969.75
	Mangrove forest	1169.51	2059.60	2595.94	1876.12	853.81	2400.76	3025.95	2186.89
	Tidal flat	53.35	92.83	116.48	83.62	38.95	108.21	135.78	97.47
KP	Salt marsh	561.83	1177.92	1168.17	795.11	410.17	1373.03	1361.67	926.82
	Mangrove forest	0.00	0.00	0.00	0.00	0.00	0.00	0.00	0.00
	Tidal flat	53.47	115.00	113.33	78.09	39.04	134.05	132.11	91.03
Kyushu	Salt marsh	528.11	1083.90	1242.71	705.26	385.55	1263.45	1448.56	822.08
	Mangrove forest	0.00	0.00	0.00	0.00	0.00	0.00	0.00	0.00
	Tidal flat	52.92	105.71	120.93	68.68	38.64	123.22	140.96	80.06

Reference

Amedro, D., Berasategui, M., Bunkan, A. J. C., Pozzer, A., Lelieveld, J., and Crowley, J. N.: Kinetics of the OH+NO_2 reaction: effect of water vapour and new parameterization for global modelling, Atmospheric Chem. Phys., 20, 3091–3105, https://doi.org/10.5194/acp-20-3091-2020, 2020.

Chen, D., Wang, X., Li, Y., Lang, J., Zhou, Y., Guo, X., and Zhao, Y.: High-spatiotemporal-resolution ship emission inventory of China based on AIS data in 2014, Sci. Total Environ., 609, 776–787, https://doi.org/10.1016/j.scitotenv.2017.07.051, 2017.

Clough, S. A., Shephard, M. W., Mlawer, E. J., Delamere, J. S., Iacono, M. J., Cady-Pereira, K., Boukabara, S., and Brown, P. D.: Atmospheric radiative transfer modeling: a summary of the AER codes, J. Quant. Spectrosc. Radiat. Transf., 91, 233–244, https://doi.org/10.1016/j.jqsrt.2004.05.058, 2005.

Fahey, K. M., Carlton, A. G., Pye, H. O. T., Baek, J., Hutzell, W. T., Stanier, C. O., Baker, K. R., Appel, K. W., Jaoui, M., and Offenberg, J. H.: A framework for expanding aqueous chemistry in the Community Multiscale Air Quality (CMAQ) model version 5.1, Geosci. Model Dev., 10, 1587–1605, https://doi.org/10.5194/gmd-10-1587-2017, 2017.

Fan, Q., Zhang, Y., Ma, W., Ma, H., Feng, J., Yu, Q., Yang, X., Ng, S. K. W., Fu, Q., and Chen, L.: Spatial and Seasonal Dynamics of Ship Emissions over the Yangtze River Delta and East China Sea and Their Potential Environmental Influence, Environ. Sci. Technol., 50, 1322–1329, https://doi.org/10.1021/acs.est.5b03965, 2016.

Feng, J., Zhang, Y., Li, S., Mao, J., Patton, A. P., Zhou, Y., Ma, W., Liu, C., Kan, H., Huang, C., An, J., Li, L., Shen, Y., Fu, Q., Wang, X., Liu, J., Wang, S., Ding, D., Cheng, J., Ge, W., Zhu, H., and Walker, K.: The influence of spatiality on shipping emissions, air quality and potential human exposure in the Yangtze River Delta/Shanghai, China, Atmospheric Chem. Phys., 19, 6167–6183, https://doi.org/10.5194/acp-19-6167-2019, 2019.

Kain, J. S.: The Kain–Fritsch Convective Parameterization: An Update, 2004.

Lana, A., Bell, T. G., Simó, R., Vallina, S. M., Ballabrera-Poy, J., Kettle, A. J., Dachs, J., Bopp, L., Saltzman, E. S., Stefels, J., Johnson, J. E., and Liss, P. S.: An updated climatology of surface dimethlysulfide concentrations and emission fluxes in the global ocean, Glob. Biogeochem. Cycles, 25, https://doi.org/10.1029/2010GB003850, 2011.

Li, C., Borken-Kleefeld, J., Zheng, J., Yuan, Z., Ou, J., Li, Y., Wang, Y., and Xu, Y.: Decadal evolution of ship emissions in China from 2004 to 2013 by using an integrated AIS-based approach and projection to 2040, Atmospheric Chem. Phys., 18, 6075–6093, https://doi.org/10.5194/acp-18-6075-2018, 2018.

Pleim, J. and Ran, L.: Surface Flux Modeling for Air Quality Applications, Atmosphere, 2, 271–302, https://doi.org/10.3390/atmos2030271, 2011.

Pleim, J. E.: A Combined Local and Nonlocal Closure Model for the Atmospheric Boundary Layer. Part I: Model Description and Testing, J. Appl. Meteorol. Climatol., 46, 1383, https://doi.org/10.1175/JAM2539.1, 2007.

Pleim, J. E., Ran, L., Saylor, R. D., Willison, J., and Binkowski, F. S.: A New Aerosol Dry Deposition Model for Air Quality and Climate Modeling, J. Adv. Model. Earth Syst., 14, e2022MS003050, https://doi.org/10.1029/2022MS003050, 2022.

Sarwar, G., Gantt, B., Foley, K., Fahey, K., Spero, T. L., Kang, D., Mathur, R., Foroutan, H., Xing, J., Sherwen, T., and Saiz-Lopez, A.: Influence of bromine and iodine chemistry on annual, seasonal, diurnal, and background ozone: CMAQ simulations over the Northern Hemisphere, Atmos. Environ., 213, 395–404, https://doi.org/10.1016/j.atmosenv.2019.06.020, 2019.

Tang, W., Yang, K., Qin, J., Li, X., and Niu, X.: A 16-year dataset (2000–2015) of high-resolution (3 h, 10 km) global surface solar radiation, Earth Syst. Sci. Data, 11, 1905–1915, https://doi.org/10.5194/essd-11-1905-2019, 2019.

U.S. EPA: CMAQ Model Version 5.3 Input Data: 1/1/2016–12/31/2016 12 km CONUS [Data set], 2019.

Xiu, A. and Pleim, J. E.: Development of a Land Surface Model. Part I: Application in a Mesoscale Meteorological Model., J. Appl. Meteorol., 40, 192–209, https://doi.org/10.1175/1520-0450(2001)040<0192:DOALSM>2.0.CO;2, 2001.

Xu, L., Pye, H. O. T., He, J., Chen, Y., Murphy, B. N., and Ng, N. L.: Experimental and model estimates of the contributions from biogenic monoterpenes and sesquiterpenes to secondary organic aerosol in the southeastern United States, Atmospheric Chem. Phys., 18, 12613–12637, https://doi.org/10.5194/acp-18-12613-2018, 2018.

Yuan, Y., Zhang, Y., Mao, J., Yu, G., Xu, K., Zhao, J., Qian, H., Wu, L., Yang, X., Chen, Y., and Ma, W.: Diverse changes in shipping emissions around the Western Pacific ports under the coeffect of the epidemic and fuel oil policy, Sci. Total Environ.,

879, 162892, https://doi.org/10.1016/j.scitotenv.2023.162892, 2023.

Zhao, J., Zhang, Y., Patton, A. P., Ma, W., Kan, H., Wu, L., Fung, F., Wang, S., Ding, D., and Walker, K.: Projection of ship emissions and their impact on air quality in 2030 in Yangtze River delta, China, Environ. Pollut., 263, 114643, https://doi.org/10.1016/j.envpol.2020.114643, 2020.